

A laboratory study on the loading and motion of a heaving box

Marcos Rodríguez, Johannes Spinneken*

Imperial College London, Department of Civil and Environmental Engineering, London SW7 2AZ, UK

Abstract

This paper concerns the nonlinear loading and dynamic response of a heaving rectangular box in two dimensions, using a series of experimental tests in regular and irregular wave conditions. Nonlinear forcing components are found to make major contributions to both the excitation problem and the motion response. Two main sources of nonlinearity are established: the first associated with higher-order wave-structure interactions, and the second associated with viscous dissipation. The present work quantifies the relative influence of these two sources. Adopting a series of regular wave cases, the first source, prevalent in steep wave conditions, is shown to be particularly significant in the diffraction regime, leading to significant excitation force amplifications. In deep water, these nonlinearities are primarily driven by interactions between incident and reflected wave components. The second source, due to vortex shedding, plays a minor role in the excitation problem, but has a major influence on the motion response. Vortex-induced effects are particularly important when the structure exhibits large motions, for example at resonance. To characterise the response in irregular waves, experimental data are provided comprising in excess of 100,000 individual waves, presenting one of the most substantial data sets of this kind to date. In considering these irregular sea states, the two aforementioned sources of nonlinearity are again found to be of critical importance. While wave-induced load amplifications of up to 60% may be observed in the excitation problem, the motion response is primarily governed by vortex-induced attenuations. In order to provide practical engineering solutions, two approaches are offered. For nonlinear forcing predictions, a two parameter Weibull fit is found to be both simple and accurate. In terms of the heave motion, a computationally efficient time-domain simulation, building upon a linear hydrodynamic description and a quadratic MOJS type drag term, leads to good agreement with experimental data.

Keywords: Heaving box, floating structure, fluid loading, irregular seas, vortex shedding

*Corresponding author

Email address: j.spinneken@imperial.ac.uk (Johannes Spinneken)

1. Introduction

The accurate description of floating body hydrodynamics is challenging in a number of ways, particularly in the extreme loading regime. In essence, an extreme loading or motion description must take into account:

- (i) the nonlinearity of the incident sea state,
- (ii) the unsteadiness of the process, which often requires modelling to be undertaken for a statistically significant time interval (3-hour storm), and
- (iii) the dynamic motion response of the structure, which may in itself be nonlinear due to large motion excursions and associated vortex shedding.

In recent years, both numerical and experimental evidence have led to significant advances in the understanding of (i)–(iii) above. For example, the interplay or coupling between wave unsteadiness and wave nonlinearity is now relatively well established. Where this concerns rapid transient changes in unsteady wave groups, notable contributions include Baldock and Swan (1994) and Johannessen and Swan (2001, 2003). While the description of short wave groups is of high scientific interest, many practical problems demand statistical evidence and require long sea simulations with randomised phasing. An example of this type of approach is given in Latheef and Swan (2013), which specifically addresses the description of the largest wave crests occurring in steep sea states.

The nonlinear excitation and dynamic motion response of floating structures are also increasingly well understood. If inviscid and irrotational flow conditions can be justified, second-order (Molin, 1979; Lighthill, 1979; Eatock Taylor and Hung, 1987; Kim and Yue, 1989, 1990; Sulisz, 1993) or fully-nonlinear (Xue et al., 2001; Ferrant et al., 2003; Kashiwagi, 2000; Maiti and Sen, 2001; Bai and Eatock Taylor, 2009; Zhou et al., 2013; Spinneken et al., 2014) potential flow approaches have often proven successful. If viscous flow is considered, recent computational formulations have also enabled an increasingly more accurate description of the flow physics (Chen et al., 2014; Vire et al., 2016).

Despite these successes, the combined occurrence of (i)–(iii) above is not fully explored. From a numerical perspective, this is extremely challenging since statistically significant simulations place a very high burden on computational cost. Indeed, of the methods noted above, only second-order potential flow formulations are considered suitable for long irregular sea simulations. In contrast, the time-marching requirement associated with either fully-nonlinear potential flow models or viscous flow formulations renders simulations of this type impractical.

Both wave-induced nonlinearity and vortex shedding are considered to be important components of the problem. In the absence of any practical numerical formulation, the

present investigation relies primarily on experimental evidence. Nevertheless, in seeking to combine the advantages of numerical and experimental modelling, a twin-tracked approach is adopted. We first consider steep regular waves, where comparisons are made between new experimental data and the recently published numerical evidence of Rodríguez et al. (2016); this latter reference being cited as RSS16 hereafter. Building upon this enhanced understanding of the flow physics, irregular waves with random wave phasing are primarily considered experimentally, and comparisons are made with results from a simplified and computationally efficient time-domain simulation.

The present paper describes a quantification of the relative importance of wave-induced load amplifications and motion damping due to vortex shedding. To enable a generic description of the problem at hand, a simple two-dimensional heaving rectangular box is considered. The experimental setup is introduced in §2. The regular wave investigation, addressing the (fixed body) excitation problem and the freely heaving case, is considered in §3. Irregular waves are subsequently discussed in §4, presenting test cases relating to over 100,000 individual wave events. The engineering applications of the present findings are briefly highlighted in §5, and overall conclusions are listed in §6.

2. Experimental setup

All experimental data presented were obtained in the Long Wave Flume located in the Hydrodynamics Laboratory within the Department of Civil and Environmental Engineering at Imperial College London. The wave flume, schematically illustrated in Figure 1, is 63 m long, 2.79 m wide and $h = 1.25$ m deep. On the left-hand side of the wave flume, four absorbing flap-type wavemakers are used to produce the incident wave conditions. Wave directionality is not considered, so that the demand to all four wavemakers was identical in all test cases. On the right hand side, a highly optimised parabolic beach minimised wave reflections contaminating the flume, which is particularly relevant in the context of irregular sea simulations.

A rectangular box was placed approximately in the centre of the wave flume, at $x = 29$ m, where $x = 0$ defines the location of the wavemakers. The experimental investigation seeks to achieve almost two-dimensional flow conditions. For this purpose, the width of the rectangular box was chosen as 2.76 m, leaving only a very small gap of 0.015 m to either of the flume's side walls. We consider a single box geometry of beam $b = 0.2h$, draught $d = b$ and mass (per unit width) $M = 2\rho bd$. This geometry was motivated by the work in RSS16, where the present geometry is referred to as box RB2. In the context of RSS16, this box geometry led to the observation of very pronounced nonlinearity due to wave-induced forcing. The submerged corners of the box were designed as two plastic sheets intersecting

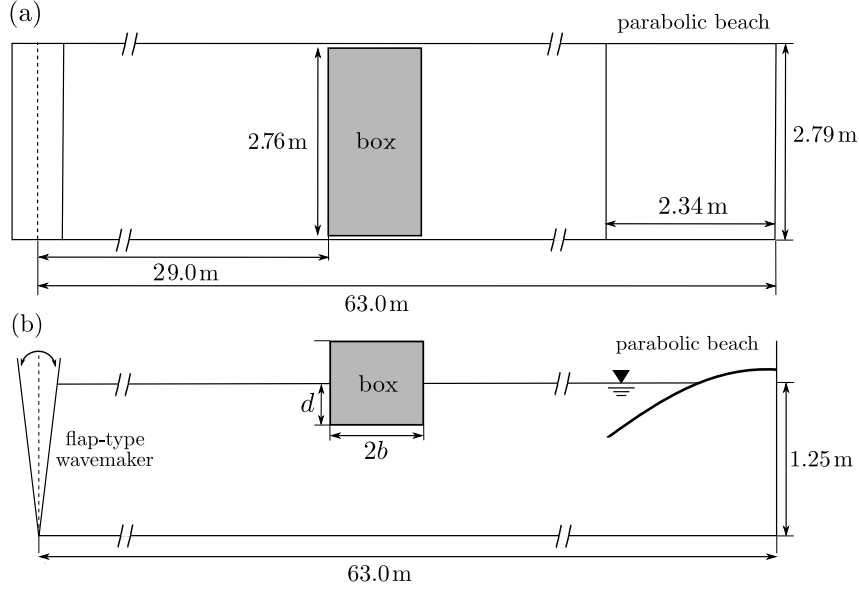


Figure 1: Schematic of the wave flume setup: (a) plan view and (b) side elevation.

at 90 degrees, with no attempt being made to round the sharp edges. Whilst this may be unrealistic (and undesirable) for a marine structure, this geometry was chosen to enable comparison with results from a number of existing investigations including Sulisz (1993) and RSS16. In terms of damping due to vortex shedding, the sharp corner case may be considered as the limiting or extreme case. Experimental data were obtained from two distinct box setups: the first related to heave excitation and the second concerned free-heave motion. For the excitation problem, the box was held fixed and the load was recorded by a pair of S-type load cells. Removing these load cells allows the box to heave freely, with all other degrees of freedom constrained; the heave motion being recorded by a high precision laser displacement sensor. Further detail of the heave motion apparatus and the sensor arrangement are provided in Appendix A.

3. Forcing and motion in regular waves

3.1. Introduction and test cases

The regular wave conditions are summarised in Table 1, providing both a set of base cases and an extended set investigating the effect of the wave steepness. To address a wide range of practically relevant wave conditions, regular incident waves of $0.2 \leq kb \leq 1.2$ were considered. The wavenumber k is expressed as the solution to $\omega^2 = gk \tanh kh$, where $\omega = 2\pi/T$ is the wave frequency and T is the wave period. Denoting the incident wave amplitude as A_I , the base cases concern a steepness of $A_I k = 0.05$ and $A_I k = 0.10$. For the purpose of the extended test cases, the steepness is extended up to $A_I k = 0.18$ for $kb = 0.6$

(Table 1). Some of the cases for low kb could not be achieved, simply due to the stroke limitations of the wavemakers. Furthermore, the maximum wave steepness ($A_I k = 0.18$) was limited by the sizing of the upstream face of the box as well as the maximum permissible horizontal load. The cases noted in Table 1 are comparable to those investigated numerically in RSS16, and reference to the corresponding numerical results is made where appropriate.

Table 1: Test cases for regular wave experiments.

Base test cases		Effect of steepness	
kb	$A_I k$	kb	$A_I k$
0.2	0.05	0.6	0.04
0.3	0.05	0.6	0.06
0.4	0.05, 0.10	0.6	0.08
0.5	0.05, 0.10	0.6	0.10
0.6	0.05, 0.10	0.6	0.12
0.7	0.05, 0.10	0.6	0.14
0.8	0.05, 0.10	0.6	0.16
0.9	0.05, 0.10	0.6	0.18
1.0	0.05, 0.10	-	-
1.1	0.05, 0.10	-	-
1.2	0.05, 0.10	-	-

3.2. Excitation forcing

For the purpose of the excitation problem, the load cells were connected as outlined in Appendix A. Figure 2 provides sample time-histories of the normalised vertical excitation force, $F(t)/(\rho g A_I b)$, for three cases: (a) $kb = 0.4$, (b) $kb = 0.7$, and (c) $kb = 1.0$. In all three cases, the wave steepness is $A_I k = 0.10$. The figure makes a direct comparison between the experimental data (black lines) and calculations based upon the semi-analytical second-order diffraction solution by Sulisz (1993) (grey lines). It is evident from the vertical asymmetry of the force traces that significant nonlinearities are present, particularly for $kb = 0.7$ and 1.0 . Overall, the agreement between the experimental results and the second-order diffraction solution is good. In fact, the data presented provide an experimental validation of the existence of very pronounced nonlinear forcing terms in both intermediate and deep water conditions. Such forcing terms have been established semi-analytically in Sulisz (1993) and numerically in RSS16, but their experimental validation to date was very limited.

The magnitude of the experimental force time-histories is slightly lower than those predicted by the analytical solution. To investigate these departures further, the first- and second-harmonic components of the experimental force traces were calculated for all base cases noted in Table 1. The results of this analysis are illustrated in Figures 3(a) and 3(b), concerning the first harmonic force, $F^{(1)}$, and the second harmonic force, $F^{(2)}$, respectively. The corresponding analytical solution of the first- and second-order problems by

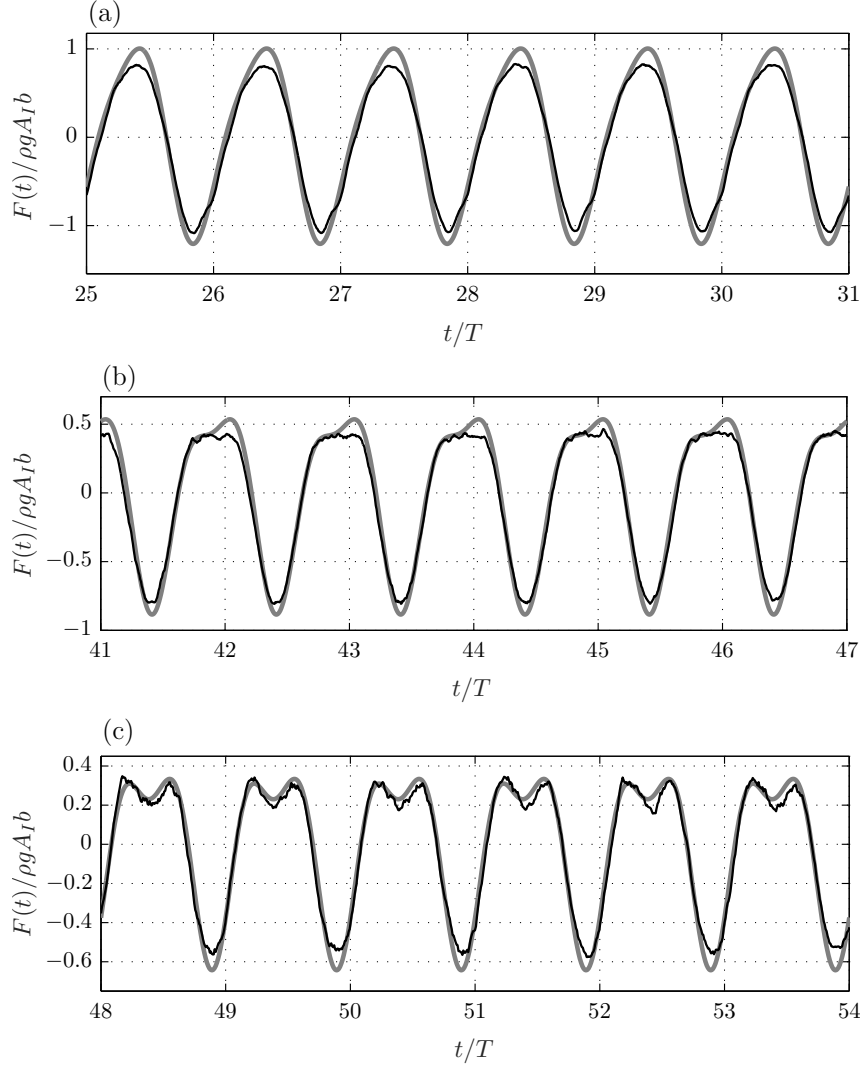


Figure 2: Time-history of the vertical excitation force due to regular waves with $A_I k = 0.10$ and (a) $kb = 0.4$, (b) $kb = 0.7$ and (c) $kb = 1.0$ showing **—** experimental data and **—** Sulisz (1993).

Sulisz (1993) is also shown (solid line). Figure 3 confirms that the magnitude of the experimentally observed forcing is consistently lower than predicted analytically. To quantify this, the dashed line in Figure 3(a) represents 90% of the predicted value of the first-order forcing. This simple approximation can be considered a good fit for $0.2 \leq kb \leq 0.8$, whereas the departure is less than 10% in the range $0.8 < kb \leq 1.2$.

The second-harmonic forcing is also compared against 90% of the corresponding analytic prediction (dashed line in Figure 3(b)). Within the range $0.2 \leq kb \leq 0.8$, this latter comparison again provides a convincing fit. As a result, it can be argued that the relative ratio between the first- and second-harmonic forcing components is maintained. As a consequence, their magnitude reduces in equal proportions, and not proportionally to their order.

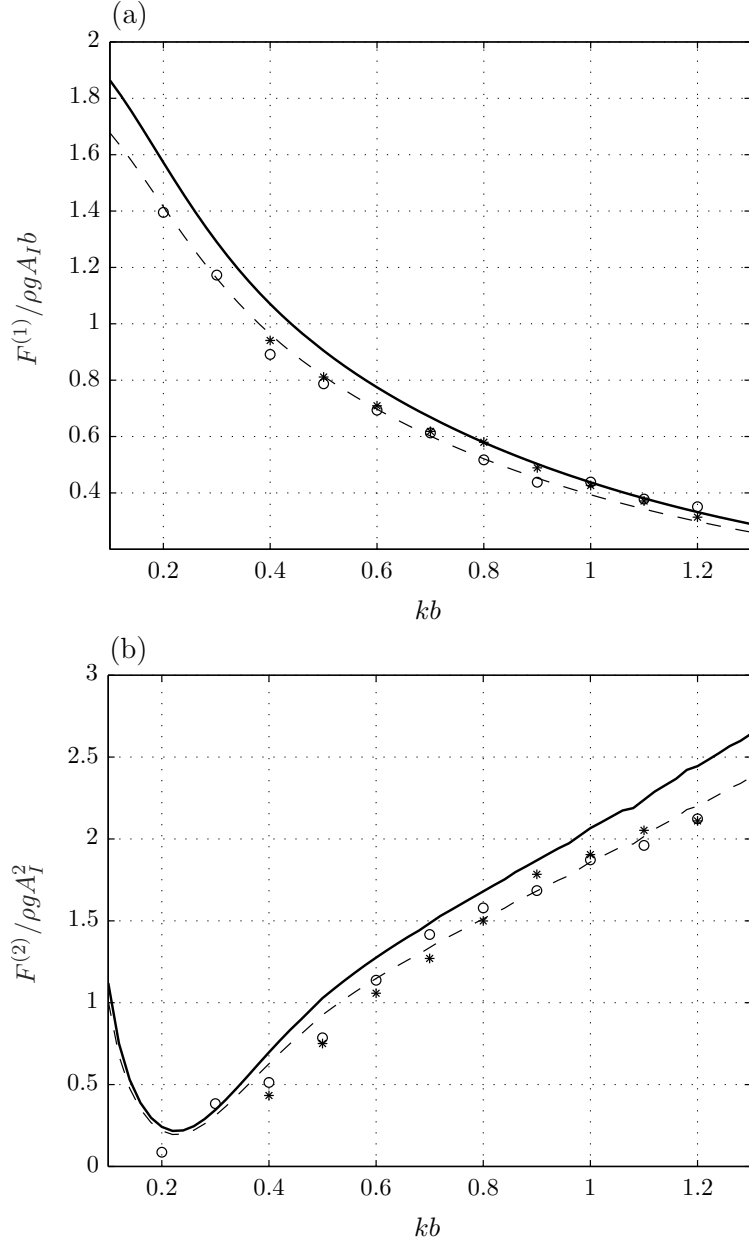


Figure 3: Normalised (a) first-harmonic and (b) second-harmonic vertical forces due to incident regular waves of steepness $A_I k = \circ$ 0.05 and $*$ 0.10, compared against **—** Sulisz (1993) and **- -** 90% of Sulisz (1993).

Considering the above evidence, the physics underpinning the force attenuations may be interpreted as follows. First, it should be noted that the forcing at both the first- and the second-harmonic is directly associated with corresponding pressure field components. If the total pressure field was attenuated globally (throughout the fluid column), then an attenuation by a factor of 0.9 in the component leading to $F^{(1)}$ should lead to an attenuation of order $(0.9)^2 = 0.81$ in the component associated with $F^{(2)}$. However, given that this is not the case, the pressure field components are believed solely to experience local attenuations.

Table 2: Comparison of first-harmonic and second-harmonic excitation forces providing the theoretical prediction (subscript th) by Sulisz (1993) and experimental data (subscript ex) with $0.04 \leq A_I k \leq 0.18$.

$A_I k$	$F_{th}^{(1)}$ [N]	$F_{ex}^{(1)}$ % diff	$F_{th}^{(2)}$ [N]	$F_{ex}^{(2)}$ % diff	$F_{th}^{(2)}/F_{th}^{(1)}$	$F_{ex}^{(2)}/F_{ex}^{(1)}$ % diff
0.04	32.4	-15.64	3.52	-14.04	0.109	+1.90
0.06	48.6	-13.41	7.92	-19.38	0.163	-6.90
0.08	64.8	-13.62	14.09	-18.03	0.217	-5.10
0.10	81.0	-10.01	22.01	-17.07	0.272	-7.84
0.12	97.2	-12.53	31.69	-18.47	0.326	-6.80
0.14	113.4	-12.90	43.14	-21.88	0.381	-10.31
0.16	129.6	-12.12	56.34	-23.20	0.435	-12.61
0.18	145.7	-11.27	71.31	-27.36	0.489	-18.14

These local attenuations appear to be relatively independent of the order (or harmonic) of the oscillation.

It should also be noted that the form of Figure 3(b) is very similar to Figure 6 in RSS16, and the reader is referred to RSS16 for additional physical explanation concerning the second-harmonic forcing drivers. Table 2 provides additional quantitative evidence relating to the extended set of test cases for $kb = 0.6$ and $0.04 \leq A_I k \leq 0.18$. The table includes both the theoretical predictions (subscript th) after Sulisz (1993) and the experimental observations (subscript ex), where the latter is expressed as a percentage difference of the former. For these cases, the experimental first-harmonic force is approximately 10%–15% lower. As the wave steepness increases beyond $A_I k = 0.12$ the second-harmonic is attenuated more heavily (Table 2), and the reduction in the second-harmonic component for the steepest wave case ($A_I k = 0.18$) is up to 27.4%. This is likely to be associated with larger local velocities arising at these higher frequency oscillations, although the exact reasons for this observation would need to be ascertained through local pressure and velocity measurements. Part of the energy contained may also be transferred to higher harmonics. Indeed, the magnitude of the third-harmonic forcing frequency for the case with $kb = 0.6$ and $A_I k = 0.18$ is approximately 5% of the first-harmonic forcing. The total energy balance of the problem will be addressed in further detail in the context of the irregular sea state investigation, §4.

3.3. Heave motion observations

The load cells were now removed as outlined in Appendix A, and the heave motion was recorded for the complete set of regular wave cases, $0.2 \leq kb \leq 1.2$. The first harmonic of the heave displacement, $\xi^{(1)}$, was used to calculate the RAO as $\xi^{(1)}/A_I$. This RAO is shown in Figure 4, where the experimental data (discrete points) are compared against a linear potential flow prediction (solid line) and a time-domain (TD) simulation incorporating an additional damping term (dashed and dash-dotted lines). The linear potential flow prediction was obtained by solving the frequency-domain equation of motion using WAMIT (2013).

For the purpose of the TD simulation, the hydrodynamic coefficients were taken from WAMIT (2013), and expressed as an Impulse Response Function (IRF) of the hydrodynamic system (Jefferys, 1984). Adopting a single convolution operation between this IRF and the heave velocity, the radiation problem may readily be expressed in the time domain. The linear excitation forcing applied to the TD model was also taken from WAMIT (2013). In the context of regular waves, a damping term could also be introduced in WAMIT (2013). However, this becomes more difficult in the irregular wave investigation, §4. To ensure that the regular wave data are entirely comparable to the irregular wave investigation, the same TD simulation approach was adopted for both. Indeed, TD simulations of this form are now commonly adopted in industry, allowing for a robust treatment of the linearised hydrodynamics, while also incorporating additional nonlinear forcing terms such as drag. Examples of this type of formulation are given in Alves et al. (2011) or Guérinel et al. (2013).

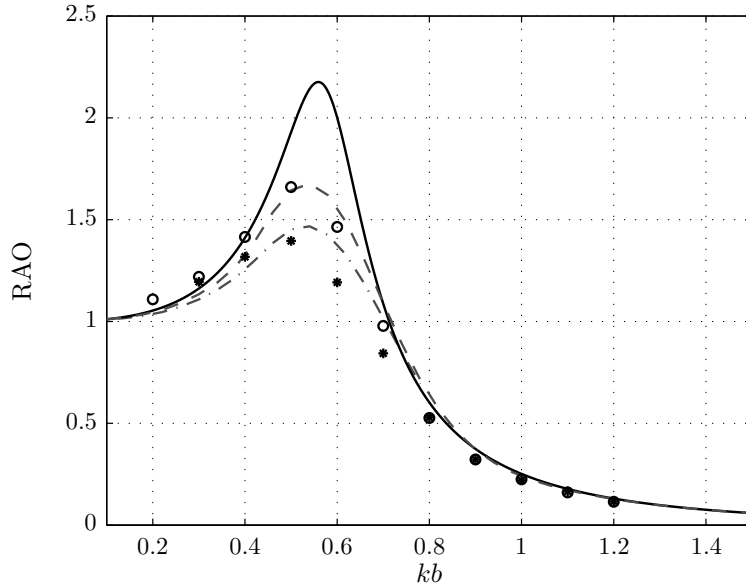


Figure 4: Heave Response Amplitude Operator (RAO) showing experimental data due to incident waves of steepness $A_I k = \circ$ 0.05 and $*$ 0.10, **—** Linear potential flow prediction (WAMIT), and TD simulation with $C_D = 350 \text{Ns}^2/\text{m}^2$ for **- -** $A_I k = 0.05$ and **- . -** $A_I k = 0.10$.

In considering the RAO in Figure 4, the agreement between the experimental data and the linear potential flow prediction is good for cases that are not in proximity of the box resonance frequency. However, for any cases in proximity of the resonance, substantial motion reductions are observed. Under resonance, the buoyancy (spring) and mass (inertia) components approximately cancel, and the system dynamics (and motion excursion) are primarily governed by the damping of the system. The observed motion reductions imply that an additional source of damping is present. The difference between the two wave steepnesses ($A_I k = 0.05$ with symbol \circ and $A_I k = 0.10$ with symbol $*$) also indicates that

this additional damping term is nonlinear, and increases with $A_I k$.

The effect of reduced motions at resonance is well known and has, for example, been reported by Salvesen et al. (1970), Downie et al. (1988), Yeung and Ananthakrishnan (1992) and Yeung and Jiang (2014). The reduced motion is generally associated with the formation of vortex structures in the vicinity of the moving body, particularly at sharp edges. A detailed treatment of the vortex-induced flow field lies outside the scope of the present work. Instead, the analysis that follows focuses on the importance of nonlinearity *in the presence* of viscous damping, where the viscous damping term is accounted for in a MOJS-type approach (Morison et al., 1950). Within the present TD simulation, the viscous damping term was introduced as a force component of the form $-C_D \dot{\xi} |\dot{\xi}|$, where C_D is a damping coefficient and $\dot{\xi}$ is the heave velocity. A value of $C_D = 350 \text{Ns}^2/\text{m}^2$ (per unit width of box) was determined empirically as a best fit to the experimental data. The good match of the TD RAO and the experimental data in Figure 4 indicates that this procedure is indeed adequate. A single constant damping coefficient C_D was used for both wave steepnesses $A_I k$. The difference between the two cases arises due to the increase of the heave velocity with wave steepness, affecting the damping force as the square of the heave velocity, $\dot{\xi} |\dot{\xi}|$.

3.4. Second-harmonic heave motion content

Figure 5 concerns the ratio of the second to the first harmonic of the box heave displacement. The figure includes both the experimental data (discrete points) and a numerical prediction presented as polynomial fits (second-order Gaussian) to the data previously reported as Figure 13(b) in RSS16. The data representation chosen for Figure 5, $\xi^{(2)}/\xi^{(1)}$, is dimensionless in terms of units, but not in terms of the order involved. As a result, the data corresponding to cases with $A_I k = 0.05$ (symbol \circ) and $A_I k = 0.10$ (symbol $*$) lie approximately a factor of two apart. The ‘*U-shaped*’ pattern observed in Figure 5 is very similar to that established computationally (Figure 13(a) in RSS16). Indeed, the experimental results confirm that the second-harmonic motion content remains small in the intermediate wave regime ($0.4 < kb < 0.8$) and increases for $kb < 0.4$ and $kb > 0.8$. The second-harmonic content observed in the diffraction regime ($kb > 0.8$) is very similar to that established numerically. This nonlinear motion content accounts for approximately 8-11% of the first harmonic motion, and underpins the importance of the interaction between the incident and the reflected wave fields as explained in detail by RSS16.

For incident conditions in the long wave regime ($kb < 0.4$), the maximum experimentally observed second-harmonic motion content (4% for $A_I k = 0.05$ and $kb = 0.2$) is significantly smaller than the corresponding numerical prediction of 12%. The case with $kb = 0.2$ and $A_I k = 0.10$ could unfortunately not be undertaken experimentally due to motion limitations of the experimental setup. Nevertheless, the experimental data relating to $kb = 0.2$ and

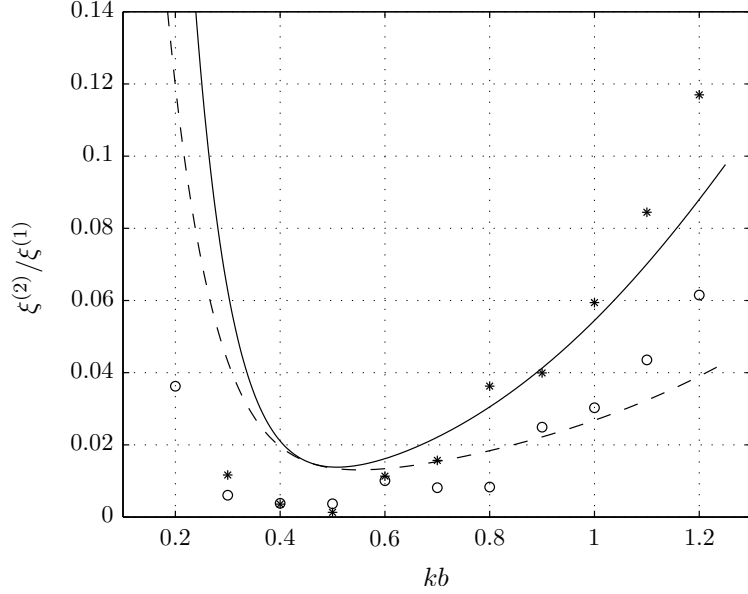


Figure 5: Normalised second-harmonic box motion $\xi^{(2)}/\xi^{(1)}$ subjected to incident regular waves of steepness $A_I k = \circ$ 0.05 and $*$ 0.10. Note: The lines represent a best fit to the numerical data from RSS16 with $A_I k = \text{---}$ 0.05 and — 0.10.

$kb = 0.3$ confirm that the nonlinear motion content in the long wave regime is much less pronounced than predicted numerically. The discussion of the numerical work in RSS16 argued that the majority of the second-harmonic motion content in the proximity of $kb = 0.2$ could be attributed to a close match of the second-harmonic forcing frequency and the resonant frequency of the box. From Figure 4, however, it is evident that large motions (or velocities) in proximity of this resonance are attenuated considerably. This is likely to also translate to an attenuation of the second-harmonic motion content for $kb \approx 0.2$, which explains the low content observed experimentally. In terms of this nonlinear motion content, the effect of the vortex-induced damping appears to be limited to the range $kb < 0.4$. Setting aside this issue, the data in Figure 5 largely confirm the findings by RSS16, underpinning the physical drivers of nonlinearity identified numerically.

3.5. Wave steepness

Figure 6 shows the second-harmonic motion content $\xi^{(2)}/\xi^{(1)}$ for three representative sets of cases with $kb = 0.2, 0.6$ and 1.0 . The maximum wave steepness possible for each case was again determined by the limitations of the experimental setup with $(A_I k)_{\max} = 0.075$ for $kb = 0.2$ and $(A_I k)_{\max} = 0.15$ for $kb = 0.6$ and 1.0 . A first observation of the data in Figure 6 confirms that the nonlinear motion content for each value of kb varies approximately linearly with $A_I k$, indicating that the underlying forcing and motion are primarily driven by second-order effects. The nonlinear motion content remains very small in the intermediate wave regime, case $kb = 0.6$ with symbol \triangle , where $\xi^{(2)}/\xi^{(1)}$ is $< 2\%$ even for $A_I k = 0.15$.

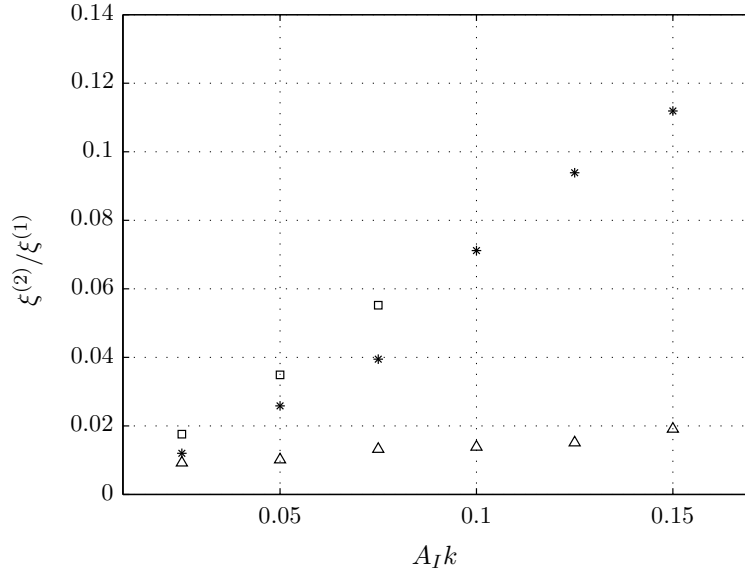


Figure 6: Normalised second-harmonic box motion $\xi^{(2)}/\xi^{(1)}$ as a function of wave steepness with $kb = \square$ 0.2, \triangle 0.6 and $*$ 1.0.

This case lies in close proximity of the box heave resonance (Figure 4), where the linearly predicted motions were attenuated by up to 30%. As a consequence, the magnitude of the vortex-induced motion reductions greatly outweighs the wave-induced motion amplifications. For both the long wave regime ($kb = 0.2$ with symbol \square) and the diffraction regime ($kb = 1.0$ with symbol $*$), the second-harmonic motion content increases consistently with $A_I k$, and reaches up to 11% for $kb = 1.0$ and $A_I k = 0.15$. In both regimes, this second-harmonic motion amplification outweighs the vortex-induced reduction observed in the first-harmonic motion (Figure 4); the latter being limited to $< 3\%$. As a result, both vortex-induced damping and wave-induced nonlinear amplifications play important roles in the motion response of the structure; their relative influence in irregular seas being considered next.

4. Forcing and motion in irregular waves

4.1. Incident wave conditions

For the purpose of the irregular wave investigation, it is important to represent the underlying energy spectrum by a realistic distribution. While a number of different distributions may be adopted, the well known JONSWAP spectrum (Hasselmann et al., 1973) is perhaps the most widely used and consequently adopted throughout the present work. The underlying energy distribution, $S_{\eta\eta}(\omega)$, for a JONSWAP spectrum is given by

$$S_{\eta\eta}(\omega) = \frac{\alpha g^2}{\omega^5} \exp\left(-\frac{5}{4} \frac{\omega_p^4}{\omega^4}\right) \gamma^\beta, \quad (1)$$

where β is defined as

$$\beta = \exp^{-\frac{(\omega - \omega_p)^2}{2\omega_p^2\sigma^2}} \quad (2)$$

with $\sigma = 0.07$ for $\omega \leq \omega_p$ and $\sigma = 0.09$ for $\omega > \omega_p$. Furthermore, $\omega_p = 2\pi f_p = 2\pi/T_p$ is the circular peak frequency, f_p is the peak frequency, T_p is the peak period, α is a gain factor, and $\gamma = 3.3$ is the peak enhancement factor. The phase of each wave component in the underlying spectrum was selected randomly from the interval $[0, 2\pi]$. The energy associated with the JONSWAP spectrum was then scaled to yield a certain significant wave height $H_s = \sqrt{4m_0}$, where m_0 is the zeroth spectral moment. The nonlinearity of the incident sea state is expressed through the parameter $\frac{1}{2}H_s k_p$, where k_p refers to the wavenumber corresponding to the peak frequency f_p . The product $\frac{1}{2}H_s k_p$ may be considered as a steepness similar to $A_I k$ in regular waves (Latheef and Swan, 2013).

In laboratory wave generation it is common practice to introduce a repeat time T_r . By ensuring that each frequency component is periodic in T_r , the entire sea state is periodic over this time window. As a result, deterministic wave generation is possible and a harmonic Fourier analysis may be performed with ease. Furthermore, the range of frequency components in the spectrum must be restricted due to limitations associated with practical wavemaking. The minimum and maximum frequencies were chosen as $f_{\min} = f_p/3$ and $f_{\max} = 3f_p$ respectively. To avoid a discontinuity in the tail of the spectrum, the last ten wave components were linearly tapered to zero.

For irregular sea simulation, the experiment must be undertaken for a sufficiently long time to obtain statistically significant data. Meanwhile, the progressive (small) build-up of wave reflections in the tank renders very long experimental runs impractical. To overcome this, each experimental run is undertaken for a repeat time of $T_r = 1500$ s. In practice, each run is undertaken for a slightly extended duration (an additional 50 s) to allow all wave components to reach the box before data sampling commences. A number of independent runs, each with a unique seed for the random phasing, are then amalgamated to obtain the overall statistical properties of the sea state. The success of this type of approach has previously been demonstrated by Latheef and Swan (2013) for the generation of wave crest statistics. Within the present work, sufficient individual runs were undertaken to obtain approximately 10,000 individual waves, leading to probabilities of exceedance of 10^{-4} without the need for extrapolation. This approach led to 10–12 individual runs for each sea state, each of 1550 s duration.

The irregular wave investigation principally concerns the effect of two sea state parameters: (i) the sea state steepness $\frac{1}{2}H_s k_p$ and (ii) the sea state peak frequency expressed through $k_p h$. Table 3 summarises the set of sea states considered. The above procedure was adopted for each of the cases noted in Table 3. To confirm the sea state properties in

the absence of the box, a series of incident conditions were also considered. Each of the sea states noted in Table 3 was generated in the absence of the box, and the measured values of H_s were found to lie within 2% of the prescribed values in all cases.

Table 3: Definition of sea state parameters for irregular wave testing.

Effect of steepness		Effect of peak frequency	
$k_p h$	$\frac{1}{2}H_s k_p$	$k_p h$	$\frac{1}{2}H_s k_p$
2.0	0.02	1.5	0.075
2.0	0.05	2.0	0.075
2.0	0.075	2.5	0.075
-	-	3.0	0.075

4.2. Excitation forcing as a function of the sea state steepness

The fixed box with the load cells connected was once again placed at $x = 29$ m (Figure 1). Figure 7 shows a subset of the time-history of the excitation force for a sea state with $k_p h = 2.0$ and $\frac{1}{2}H_s k_p = 0.075$. An upcrossing analysis was performed on all time-histories of the heave excitation forces. Figure 8 shows the probability Q of exceeding a certain excitation force (normalised by $\rho g H_s b$ for dimensional consistency) for irregular seas with $k_p h = 2.0$ and $0.02 \leq \frac{1}{2}H_s k_p \leq 0.75$. Within the upcrossing analysis, both local maxima and local minima were obtained, and are shown by the thin and thick lines respectively. In addition to the experimental data, the linear potential flow prediction is also shown. Within this linear description, the statistics of the force maxima and force minima are identical, and this solution is hence shown as a single grey line. In contrast, the presence of nonlinearity leads to distinctly different force minima and force maxima in the experimental observations.

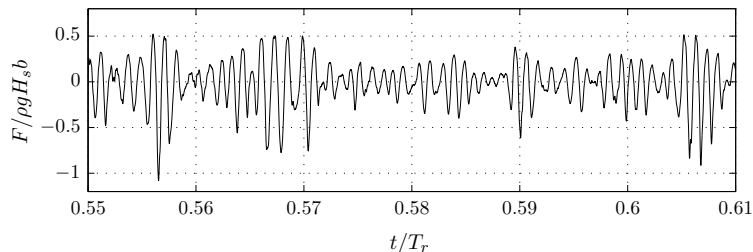


Figure 7: Sample time-history of the heave excitation force in an irregular sea state with $k_p h = 2.0$ and $\frac{1}{2}H_s k_p = 0.075$.

The force minima (thick lines) clearly lead to the largest overall forces. In considering the smallest amplitude sea state ($\frac{1}{2}H_s k_p = 0.02$) in Figure 8, the absolute values of the measured force minima are between 5-10% lower than the linear predictions. These departures are believed to be due to small local attenuations comparable to the regular wave excitation problem (Figure 3). In the fixed box case, these local attenuations are also of comparable magnitude to the flat-plate experiments presented by Stiassnie et al. (1984), where the

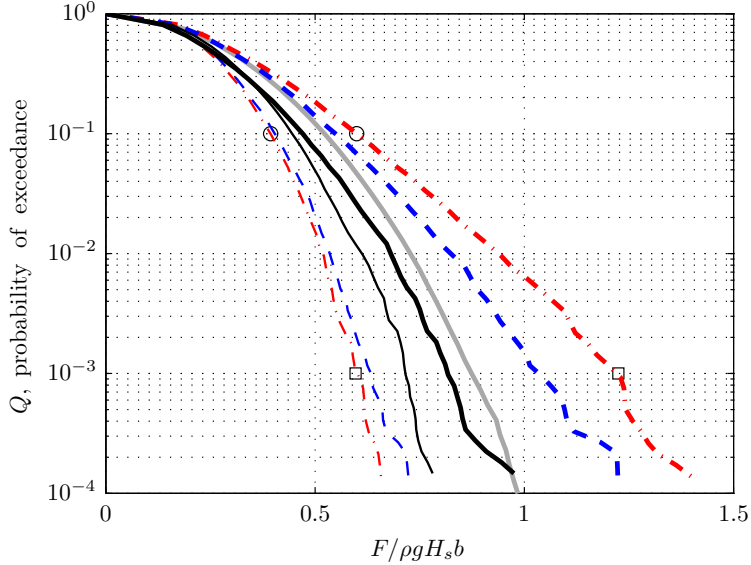


Figure 8: Probability of exceedance Q of the vertical excitation forces due to sea states with $k_p h = 2$ and $\frac{1}{2}H_s k_p =$ — 0.02, — 0.05 and - - 0.075, where the thin lines refer to local maxima and the thick lines refer to local minima, and — linear potential flow prediction.

influence due to vortex shedding was clearly established. As the significant wave height of the sea state increases ($\frac{1}{2}H_s k_p = 0.05$ and $\frac{1}{2}H_s k_p = 0.075$), the experimentally observed force minima are consistently larger than those predicted linearly. Due to the presence of significant nonlinear content, the excitation force time-histories become strongly asymmetric (see example in Figure 7), such that the local minima increase and the local maxima decrease. This is consistent with the force traces in Figure 2 in the context of regular waves, exhibiting much larger ‘troughs’ than ‘crests’. Considering Figure 8 further, the smallest amplitude event ($\frac{1}{2}H_s k_p = 0.02$) exhibits reductions of approximately 10% across all Q . In contrast, $\frac{1}{2}H_s k_p = 0.05$ and 0.075 show significant force amplifications. For $Q = 10^{-3}$, the measured forces in the most nonlinear sea state are up to 35% larger than linearly predicted.

Within Figure 8, four events are highlighted for the sea state with $\frac{1}{2}H_s k_p = 0.075$. These events relate to the force minima and maxima at $Q = 10^{-1}$ (symbol \circ) and $Q = 10^{-3}$ (symbol \square). To highlight the nonlinearities associated with these events, the corresponding experimental time-histories are shown in Figure 9. In each case, the time-history is time shifted such that the wave event of interest occurs at $t/T_p = 0$. Within Figure 9, parts (a) and (c) correspond to force maxima, and parts (b) and (d) correspond to force minima. The force minima become significantly larger in magnitude as Q decreases, while the force maxima only increase very moderately. The local force maxima in parts (a) and (c) lie within the range $0.4 \leq F/\rho g H_s b \leq 0.6$ for $10^{-1} \geq Q \geq 10^{-3}$. In marked contrast, the corresponding local force minima in parts (b) and (d) are characterised by $0.65 \leq |F/\rho g H_s b| \leq 1.25$. The extent of this asymmetry is comparable with the observations made in the context of

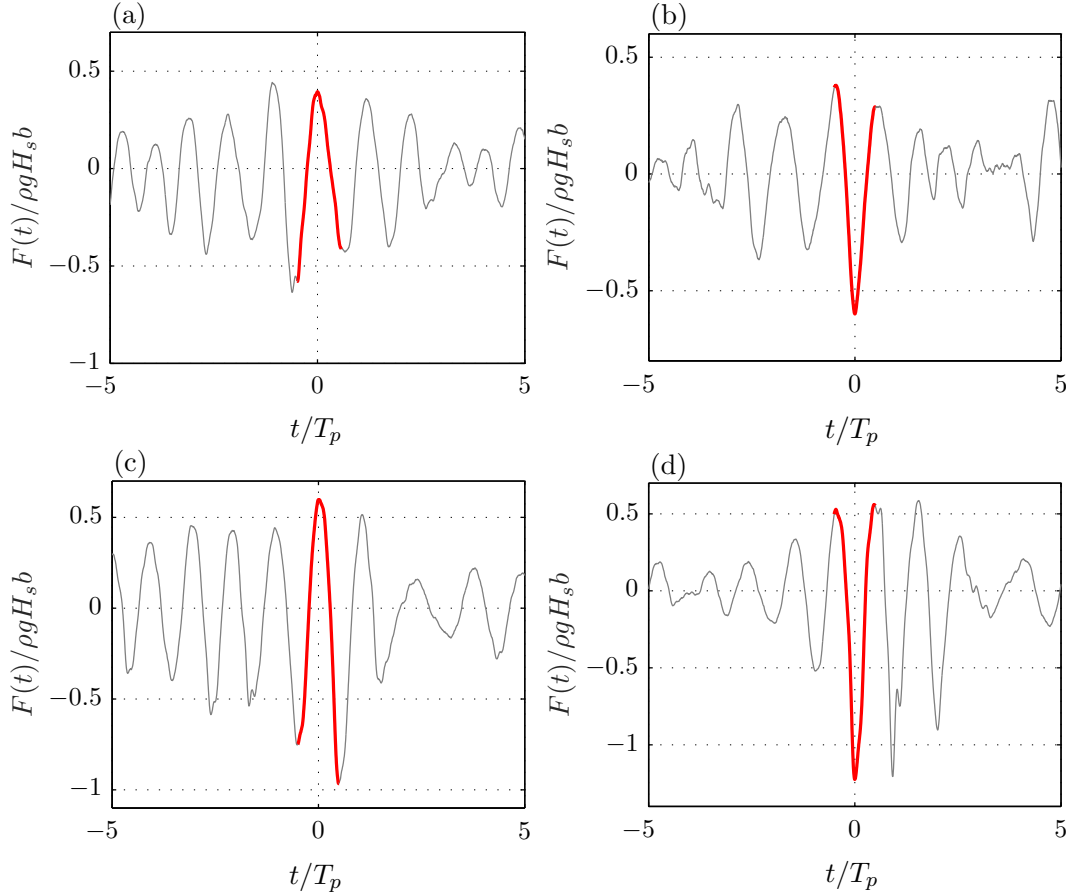


Figure 9: Heave excitation force time-histories for a sea state with $k_p h = 2.0$ and $\frac{1}{2}H_s k_p = 0.075$. The highlighted part of the time-history indicates an event corresponding to (a) maximum with $Q = 10^{-1}$, (b) minimum with $Q = 10^{-1}$, (c) maximum with $Q = 10^{-3}$ and (d) minimum with $Q = 10^{-3}$. Note: all events were time-shifted so that the event under consideration occurs at $t/T_p = 0$.

regular waves, Figure 2, where the second-harmonic forcing was clearly seen to reduce the force maxima while increasing the absolute value of the force minima.

Some differences can also be observed in the nature or shape of the irregular wave events in Figure 9. The force maxima generally occur in what can be described as a relatively narrow-banded wave event, where the time-history in the proximity of the event is relatively regular. In contrast, the force minima relate to events where a very rapid evolution of the force takes place, indicating a significantly more broad-banded behaviour in the vicinity of the event. Within this broad-banded (or focused wave group like) event, significant higher harmonic content must be present, which leads to very rapid changes in the force time-history. Importantly, this also leads to larger overall forcing for the force minima.

To investigate the nonlinear content further, a spectral analysis of the excitation forces was performed. Figure 10(a)–10(c) show the ensemble average of the harmonic content for each of the three sea states considered. In each case, this representation is obtained by averaging the harmonic content across each of the individual random phase realisations.

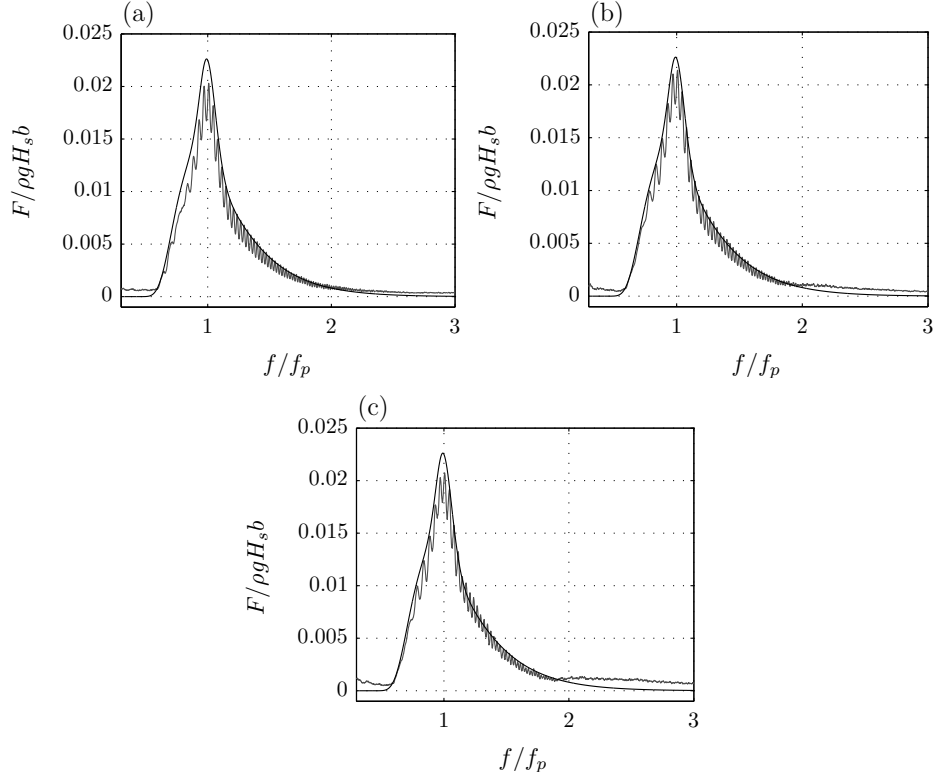


Figure 10: Harmonic content of the vertical excitation forces due to sea states with $k_p h = 2.0$ and $\frac{1}{2} H_s k_p =$ (a) 0.02, (b) 0.05 and (c) 0.075 showing — ensemble average of experimental data and — linear potential flow prediction.

This average harmonic content, shown by the grey line, is compared against the linear prediction, given by the black line. Figure 10(a) concerns the smallest amplitude wave case with $\frac{1}{2} H_s k_p = 0.02$. A reduction in the energy content is evident in vicinity of the peak frequency, while a good match can be observed towards higher frequencies. As the significant wave height increases (Figures 10(b) and 10(c)) there is a noticeable increase in energy at frequencies $f/f_p \geq 2$. This confirms that the mechanisms of second-harmonic forcing observed in the context of regular waves are also found in irregular waves. The occurrence of these higher harmonic force components leads to a local steepening of the largest excitation forces, and causes the asymmetry and force amplifications observed in Figure 8.

4.3. Excitation force as a function of sea state peak frequency

To investigate the effect of nonlinear content in the excitation forces for a wider range of peak frequencies, the range $1.5 \leq k_p h \leq 3.0$ with $\frac{1}{2} H_s k_p = 0.075$ was considered experimentally (Table 3). Figure 11 concerns the heave force probability of exceedance, expressed as the ratio of the measured force F and the linear prediction F_{lin} for $k_p h = 1.5, 2.0, 2.5$ and 3.0. The nonlinear amplifications in the excitation forces are similar for $k_p h = 1.5$ and

2.0. As $k_p h$ increases, the nonlinear amplification at $Q = 10^{-3}$ increases to approximately 45% for $k_p h = 2.5$ and 65% for $k_p h = 3.0$. A harmonic decomposition of the force traces for $k_p h = 2.5$ and $k_p h = 3.0$ was again undertaken (not shown herein), which revealed the origin of the sharp nonlinear load increase for $k_p h = 3.0$. As $k_p h$ increases, the second harmonic content becomes particularly apparent. This is entirely consistent with the trends for regular waves (Figure 3(b)), where the second-harmonic content was found to increase rapidly with kh . For $k_p h = 3.0$, there is also a notable increase in the energy content at third harmonic.

Taken as a whole, the investigation of the excitation problem in irregular seas confirmed the importance of wave-induced nonlinearities. Energy dissipation due to vortex-induced damping may lead to some reductions in the forcing; however, these reductions are greatly outweighed by the forcing increase due to wave-induced amplifications.

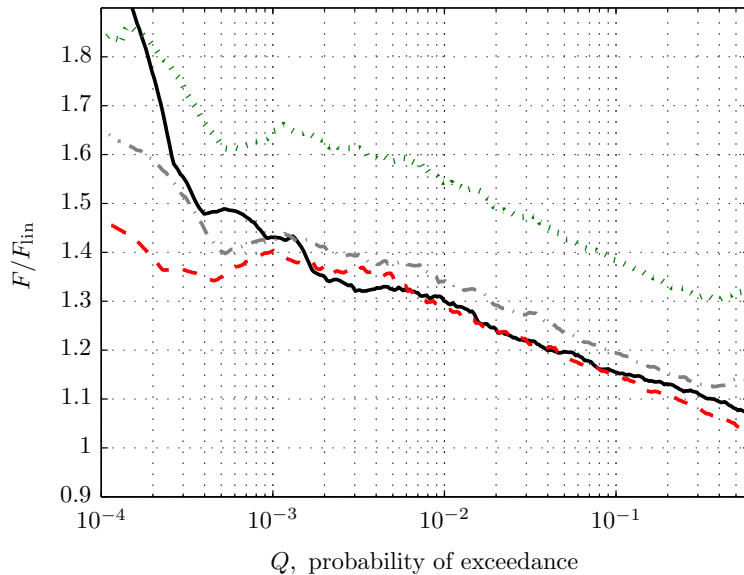


Figure 11: Amplification of the local force minima due to sea states with $\frac{1}{2}H_s k_p = 0.075$ and $k_p h =$ **—** 1.5, **- -** 2.0, **- - -** 2.5, **· · ·** 3.0.

4.4. Heave motion probability of exceedance

Once again removing the load cells, the box was now free to heave as described in Appendix A. Adopting the same incident wave conditions as for the purpose of the excitation problem (Table 3), the heave motion was recorded for the entire set of sea states. Applying an upcrossing analysis to the heave motion time-histories for all sea states with $k_p h = 2.0$ yields the probability of exceedance Q shown in Figure 12. This figure concerns three sea states with $\frac{1}{2}H_s k_p = 0.02$ (small-amplitude), 0.05 (mildly-nonlinear) and 0.075 (nonlinear). Each of these sea states was again implemented sufficiently often to obtain 10,000 individual

wave events, so that data up to $Q \approx 10^{-4}$ are available for each case. The linear analytical solution (grey line) is also shown for reference.

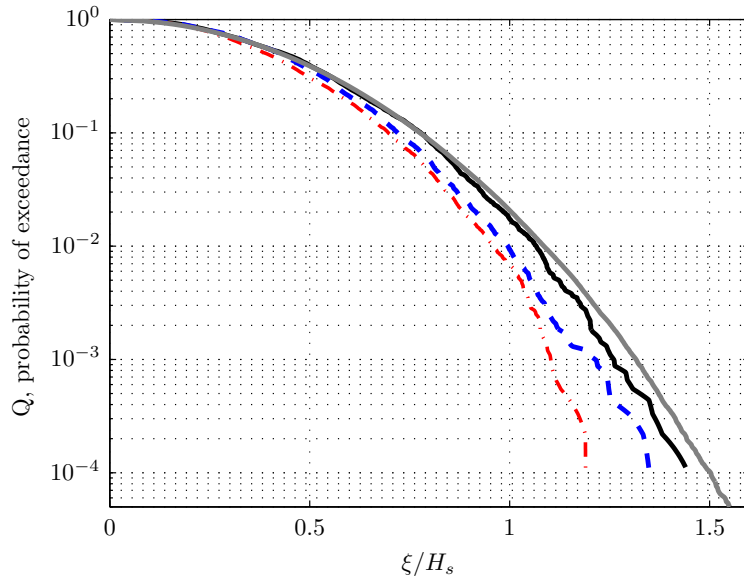


Figure 12: Probability of exceedance Q of the heave motion due to sea states with $k_p h = 2.0$ and $\frac{1}{2}H_s k_p =$ — 0.02, - - 0.05, - . - 0.075 and — linear potential flow prediction.

Considering first the smallest amplitude sea state with $\frac{1}{2}H_s k_p = 0.02$, the agreement between the measured heave displacements and the linear prediction is good (Figure 12). Indeed, at $Q = 10^{-3}$, the experimentally observed motions are only 4% smaller than predicted linearly. From the corresponding excitation problem, Figure 8, it is clear that the forcing nonlinearity of this sea state is very limited. Furthermore, given the small amplitude of the heave motions for $\frac{1}{2}H_s k_p = 0.02$, the effect of vortex-induced damping is also very limited. As a result, both forcing nonlinearity and motion damping are small, and the case with $\frac{1}{2}H_s k_p = 0.02$ closely follows the linear prediction.

As the sea state steepness increases to $\frac{1}{2}H_s k_p = 0.05$ and 0.75 , the experimentally observed heave displacements in Figure 12 become considerably smaller than the linear predictions. This is in marked contrast to the excitation forcing, Figure 8, which clearly increases with sea state steepness. The observation in Figure 12 presents a critical finding of this investigation. The excitation force is associated with significant nonlinearity and amplifications (in excess of 30% for $k_p h = 2.0$). However, these amplifications do not translate into the box displacement. In fact, the maximum heave motion *decreases* with increasing sea state steepness, despite the increasing amount of nonlinear forcing. At $Q = 10^{-3}$, the heave motion reduction compared to the linear base case accounts for up to 7% for $\frac{1}{2}H_s k_p = 0.05$ and 16% for $\frac{1}{2}H_s k_p = 0.075$. The motion reduction occurs despite a corresponding force amplification of 15% ($\frac{1}{2}H_s k_p = 0.05$) and 30% ($\frac{1}{2}H_s k_p = 0.075$). This latter reduction has two important drivers. First, the maximum heave forces are associated with considerable

higher-harmonic (nonlinear) content, which does not fully translate into motions, primarily due to the large box inertia. As inertia forcing scales with $\omega^2 M$, the resistance to motion at the second harmonic with $\omega^{(2)} = 2\omega^{(1)}$ increases significantly when compared to the first harmonic. Second, large heave motions are associated with significant vortex shedding, which reduces the most severe motion excursions.

4.5. Viscous motion damping and spectral content

Adopting the TD approach introduced in the context of regular waves (§3.3), irregular wave simulations were also undertaken. For this purpose, the quadratic viscous damping term was kept identical to that established for the regular wave RAO (Figure 4, $C_D = 350\text{Ns}^2/\text{m}^2$). Figure 13 shows the probability of exceedance of the heave motion for (a) $\frac{1}{2}H_s k_p = 0.02$ and (b) $\frac{1}{2}H_s k_p = 0.075$. In considering parts (a) and (b) of Figure 13, the TD simulation provides a good prediction of the experimentally observed probabilities. In this context, it should be stressed again that this TD simulation does not include any nonlinear excitation forcing terms; the nonlinearity of the simulation being limited to the term $C_D \dot{\xi}|\dot{\xi}|$. Apart from this term, the TD simulation relies entirely on linear potential flow quantities. Given this relative simplicity, the agreement observed in Figure 13 is remarkable.

To further establish the influence of the various forcing nonlinearities, the spectral content of the irregular sea motion response is considered in Figures 13(c) ($\frac{1}{2}H_s k_p = 0.02$) and 13(d) ($\frac{1}{2}H_s k_p = 0.075$). In close similarity to the force comparisons, an ensemble average is adopted. For dimensional consistency, the square root of the spectral density \sqrt{S} was normalised by the incident significant wave height H_s . For the small amplitude sea state with $\frac{1}{2}H_s k_p = 0.02$, Figure 13(c), the agreement between the experimental and theoretical heave motion spectra is good, except in the range $0.95 < f/f_p < 1.25$. This frequency range is equivalent to $0.37 < kb < 0.65$, corresponding to near resonant conditions (Figure 4). In the vicinity of this resonance, large box motions are clearly attenuated.

As the steepness increases, Figure 13(d), the reduction in the amplitude content in the range $0.95 < f/f_p < 1.25$ becomes more significant. This reduction is also predicted by the TD simulation, which remains in relatively good agreement with the experimental data. From the data in Figure 13(c) and (d) it is clear that the largest reductions occur near the resonance of the structure, and that this motion reduction becomes more pronounced as the sea state steepness increases. At the same time, the energy content arising at the second harmonic (for example $f/f_p = 2$ for the spectral peak) is practically negligible. Even for the largest steepness of $\frac{1}{2}H_s k_p = 0.075$, the higher harmonic motion content remains small, which is in marked contrast to the corresponding excitation force spectrum (Figure 10).

The damping introduced by viscous dissipation is closely related to the total energy contained within the box motion. In the absence of viscous damping, the work done by the

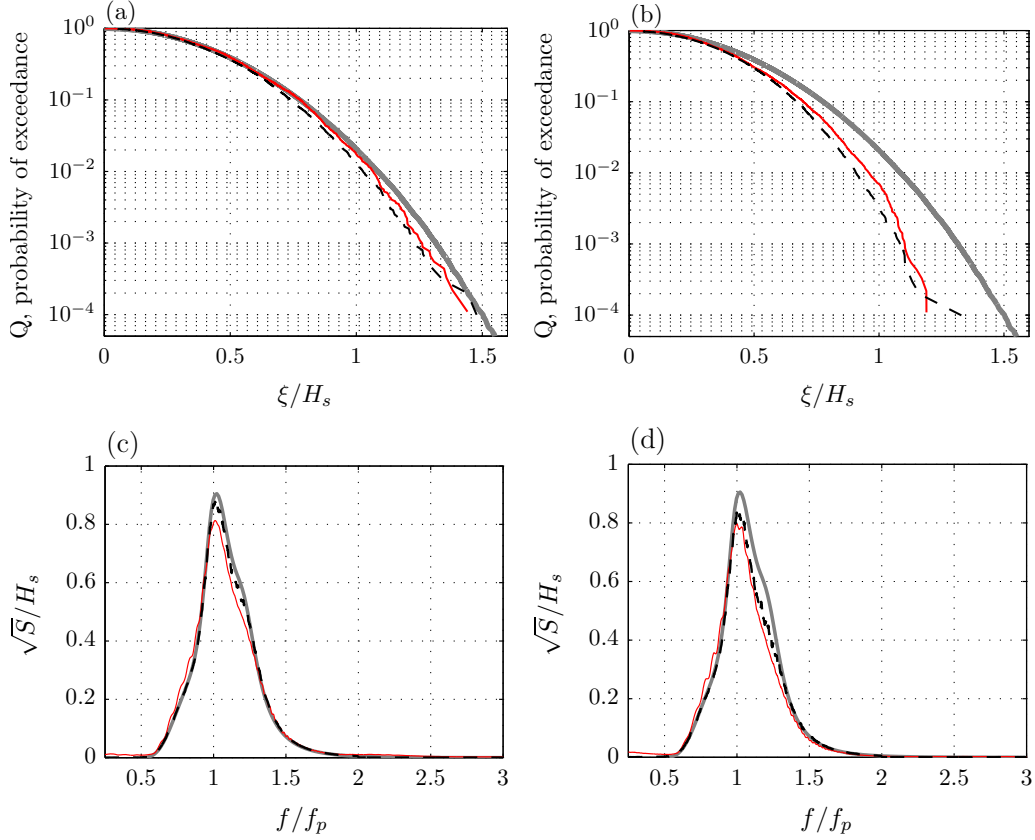


Figure 13: Sea state with $k_p h = 2.0$ with heave motion probability of exceedance for (a) $\frac{1}{2} H_s k_p = 0.02$ and (b) $\frac{1}{2} H_s k_p = 0.75$ and spectral content for (c) $\frac{1}{2} H_s k_p = 0.02$ and (d) $\frac{1}{2} H_s k_p = 0.075$, showing — linear potential flow prediction, — experimental data and - - TD simulation.

excitation forcing would directly translate into potential and kinetic energy, damped only by wave radiation. Considering the actual energy contained in the box motion can hence serve as an additional means of quantifying the viscous damping losses. The total motion energy is composed of the kinetic energy $E_k = \frac{1}{2} M \dot{\xi}^2$ and the potential energy $E_p = \frac{1}{2} k \xi^2$, where k is the spring stiffness. For a simple box geometry, the spring stiffness due to buoyancy is given by the water plane area which, expressed per unit width, is $A = 2b$. From the experimental data, E_k and E_p are readily obtained as functions of time. The total average energy \bar{E} may be expressed as the average of the sum of E_k and E_p for the entire sea state, taking into consideration approximately 10,000 wave cycles as before.

Table 4 expresses the experimentally obtained value of \bar{E} for sea states with $k_p h = 2.0$, normalised over the corresponding value for a linear simulation in the absence of viscous damping, \bar{E}_{lin} . Furthermore, Table 4 also details the TD simulation results for $C_D = 350 \text{Ns}^2/\text{m}^2$ and a variation of $\pm 20\%$ around this nominal value. For the smallest amplitude sea state with $\frac{1}{2} H_s k_p = 0.02$, the table confirms that viscous damping already plays an important role, with $\bar{E}/\bar{E}_{\text{lin}} = 0.81$ for the experimental observation. A sea state of steepness

Table 4: Energy contained in box motion

Steepness $\frac{1}{2}H_s k_p$	Experimental $\overline{E}/\overline{E}_{\text{lin}}$	TD $\overline{E}/\overline{E}_{\text{lin}}$ with $C_D = 350\text{Ns}^2/\text{m}^2 (+20\%, -20\%)$
0.02	0.81	0.84 (0.81, 0.87)
0.05	0.66	0.69 (0.66, 0.74)
0.075	0.59	0.61 (0.57, 0.66)

$\frac{1}{2}H_s k_p = 0.02$ is associated with very limited wave-induced nonlinearity, but evidently associated with considerable viscous-induced damping (Table 4). The TD simulation confirms the experimental observation and a nominal value of $C_D = 350\text{Ns}^2/\text{m}^2$ gives $\overline{E}/\overline{E}_{\text{lin}} = 0.84$. Considering a variation of $\pm 20\%$ around this nominal value leads to $\overline{E}/\overline{E}_{\text{lin}} = (0.81, 0.87)$. Very similar observations apply to the two sea states with $\frac{1}{2}H_s k_p = 0.05$ and 0.075 , where the increased importance of viscous damping leads to $\overline{E}/\overline{E}_{\text{lin}}$ as low as 0.59 (experimental) and 0.61 (TD simulation with $C_D = 350\text{Ns}^2/\text{m}^2$).

The energy-based comparisons between the TD simulation and the experimental observations confirm that viscous damping is likely to be the primary driver of motion reductions. A secondary driver may be due to wave energy transfers to higher harmonics. However, considering the combined evidence of (i) the probability of motion exceedance (Figure 13 (a)–(b)), (ii) the absence of higher harmonic box motions (Figure 13 (c)–(d)) and (iii) the significant reduction in the total box motion energy (Table 4), suggests that the majority of the motion reductions is due to additional damping. This also agrees with the regular wave observations in §3 and previous evidence such as Yeung and Ananthkrishan (1992) and Downie et al. (1988).

4.6. Identifying individual motion events

The above discussion highlighted that the motion reductions are primarily associated with attenuations close to the resonance frequency, particularly as the sea state steepness increases. To investigate this further, individual wave events of the experimental data set were analysed. For this purpose, the motion events corresponding to the local minima at $Q = 10^{-1}$ and 10^{-3} were isolated from the full sea state simulation. These events are illustrated in Figure 14, where the left hand side parts (a) and (c) correspond to $\frac{1}{2}H_s k_p = 0.02$ and the right hand side parts (b) and (d) correspond to $\frac{1}{2}H_s k_p = 0.075$. All time-histories were shifted such that the event under consideration occurs at $t/T_p = 0$.

From a qualitative perspective, there is a marked difference in the events for the two steepnesses. The events relating to the small amplitude sea state (parts (a) and (c)) resemble focused-like or broad-banded parts of the motion time-history. In contrast, the events relating to $\frac{1}{2}H_s k_p = 0.075$ (parts (b) and (d)) appear to correspond to a much more narrow-banded, regular-wave like, part of the sea state. To express this in a more convenient and

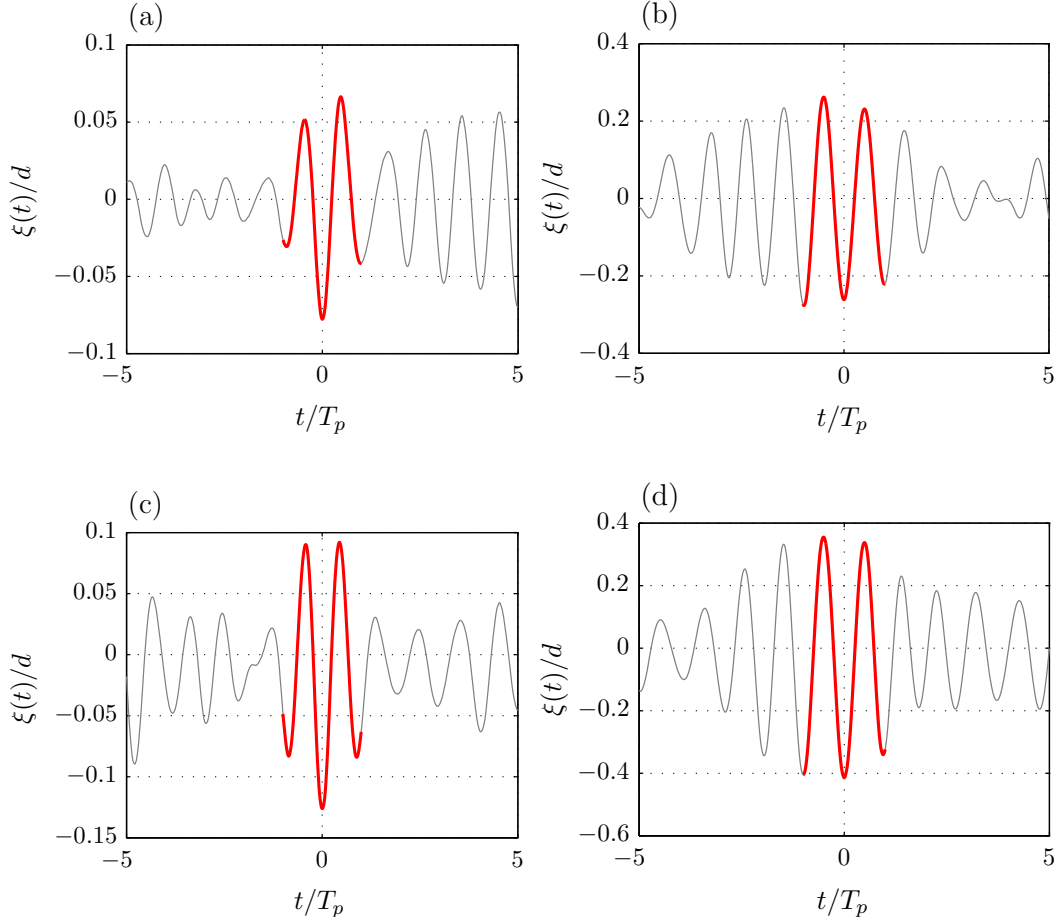


Figure 14: Heave motion time-histories due to sea states with $k_p h = 2.0$. The highlighted part of the time-history indicates an event corresponding to (a) $\frac{1}{2}H_s k_p = 0.02$ and $Q = 10^{-1}$, (b) $\frac{1}{2}H_s k_p = 0.075$ and $Q = 10^{-1}$, (c) $\frac{1}{2}H_s k_p = 0.02$ and $Q = 10^{-3}$ and (d) $\frac{1}{2}H_s k_p = 0.075$ and $Q = 10^{-3}$. Note: all events were time-shifted so that the event under consideration occurs at $t/T_p = 0$.

accessible way, a cross-correlation coefficient, R , expressed as the correlation between the highlighted part of the event and a signal $-\xi_{\max} \cos(\omega t)$ was calculated. The frequency ω was varied over the full range of sea state frequencies, and ξ_{\max} was taken as the value at $t/T_p = 0$.

This correlation coefficient R is presented in Figure 15, where the order of parts (a)-(d) is identical to that shown in Figure 14. Considering the small-amplitude sea state first, parts (a) and (c), the motion response is generally associated with a relatively broad-banded behaviour. The correlation coefficient is largest in the proximity of the spectral peak ($f/f_p = 1$), but also shows large non-zero values for $f/f_p > 1$. A second peak appears at $f/f_p \approx 1.35$, corresponding to the resonance frequency of the box. As a result, the box motion response for the small amplitude sea state is governed by both large incident wave amplitudes (the spectral peak) *and* wave components in the vicinity of the box resonance.

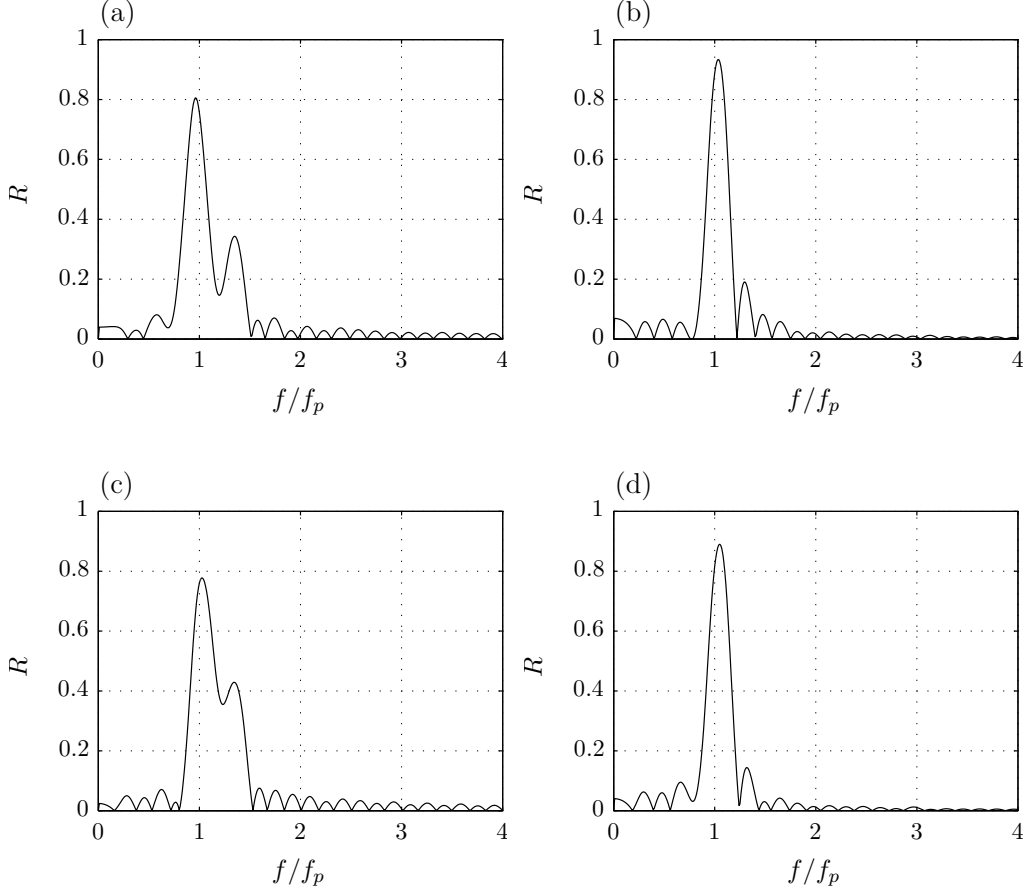


Figure 15: Cross-correlation coefficient R of the heave motion due to sea states with $k_p h = 2.0$ and (a) $\frac{1}{2}H_s k_p = 0.02$ and $Q = 10^{-1}$, (b) $\frac{1}{2}H_s k_p = 0.075$ and $Q = 10^{-1}$, (c) $\frac{1}{2}H_s k_p = 0.02$ and $Q = 10^{-3}$ and (d) $\frac{1}{2}H_s k_p = 0.075$ and $Q = 10^{-3}$.

In contrast, the motion response for the most nonlinear sea state, parts (b) and (d) with $\frac{1}{2}H_s k_p = 0.075$, is primarily governed by wave excitation close to the sea state peak frequency. For both values of Q , the correlation coefficient R is in excess of 0.9 for $f/f_p = 1$. The resonance condition is attenuated considerably, with $0.15 \leq R \leq 0.2$ close to $f/f_p = 1.35$. Taken as a whole, the motion response in a nonlinear sea state is determined by non-resonant excitation associated with wave components in proximity of f_p . The lack of large amplitude responses at higher frequencies, particularly around the box resonance, explains the narrow-banded events observed in Figure 14 (b) and (d). In physical terms, the reduced significance of the resonance is associated with the steepness-dependent damping force, $C_D \dot{\xi} |\dot{\xi}|$.

4.7. Sea state peak frequency

To investigate the effect of the sea state peak frequency, the most nonlinear sea state ($\frac{1}{2}H_s k_p = 0.075$) was considered again for $k_p h = 2.5$ and 3.0. For each of the new sea states,

a number of long duration simulations were once again generated, and the local minima of the heave motion time-histories obtained using an upcrossing analysis. Figure 16 concerns the ratio of the experimentally observed, the linearly predicted displacements, and $k_p h = 2.0$ for reference. For $k_p h = 2.0$ and 2.5, the reduction in the measured heave displacements are in the order of 20-25%, which increases up to 30% for $k_p h = 3.0$. This increase for larger $k_p h$ is consistent with the largest departures observed in the RAO in Figure 4 ($kh = 3.0$ corresponds to $kb = 0.6$). The decrease in heave motion can be attributed to increased vortex-induced damping around the box resonance.

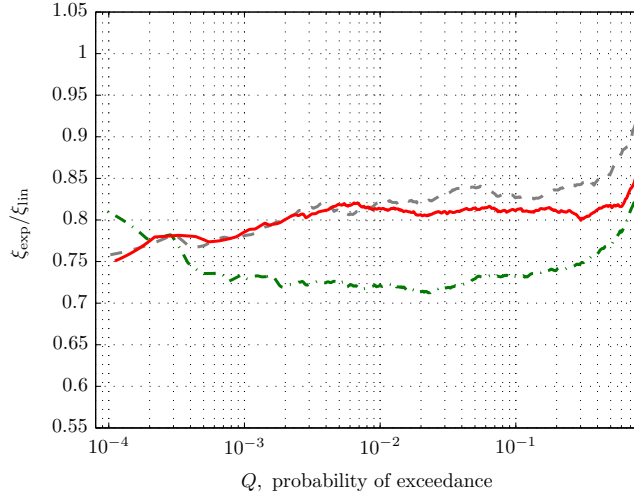


Figure 16: Ratio of measured heave displacement to theoretical potential flow prediction for probabilities of exceedance Q due to irregular sea states with $\frac{1}{2}H_s k_p = 0.075$ and $k_p h =$ — 2.0, - - 2.5, - . - 3.0.

This is further confirmed in Figure 17, showing the spectral content of the heave motion. As before, an ensemble average of individual experimental runs was obtained, yielding a single spectrum for each sea state. The regular wave analysis established that the energy content in the frequency band $0.4 < kb < 0.65$ experiences the greatest reductions; this range being indicated by the vertical lines in Figure 17. In the context of irregular waves, the reduction is seen to be particularly significant for $k_p h = 2.5$ and 3.0, since the majority of the incident wave energy lies in the critical frequency range. The TD simulation captures the majority of this reduction, although the fit for $k_p h = 3.0$ becomes less convincing. For an improved fit, the damping coefficient C_D would have to be adjusted as a function of $k_p h$. Nevertheless, Figure 17 clearly confirms that vortex-induced damping is the primary driver for motion reductions, with the second-harmonic motions once again negligible.

5. Towards engineering applications

The present findings are of relevance where large nonlinear forcing and motions are of concern. While the results presented here are specific to a two-dimensional rectangular box,

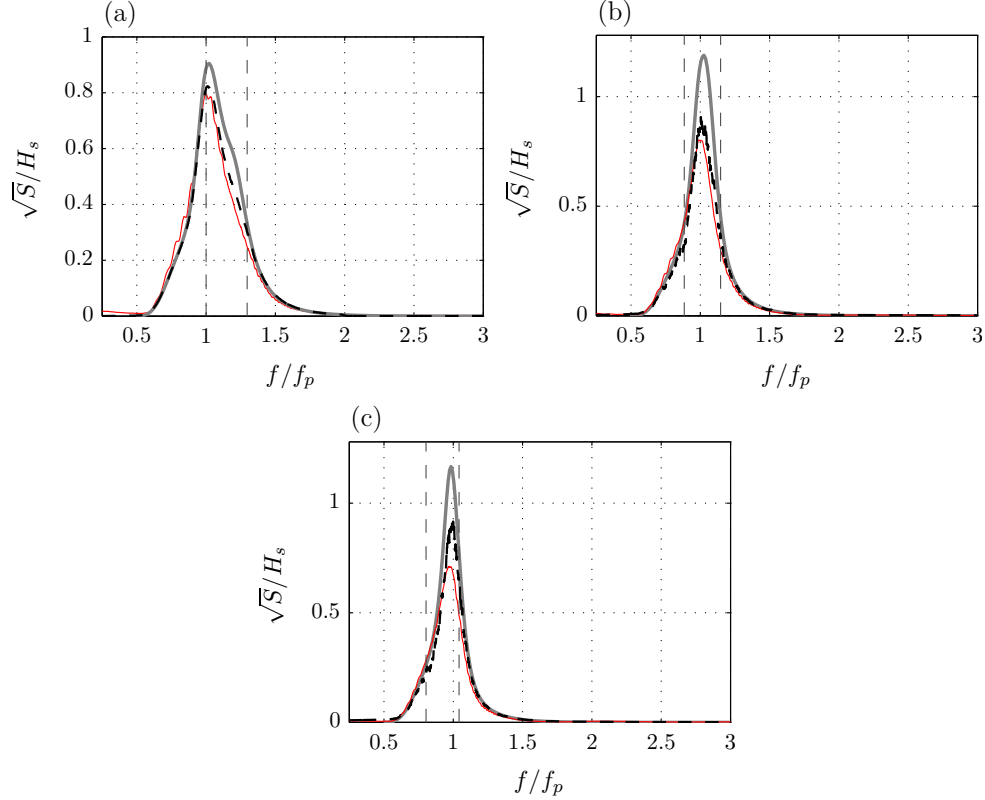


Figure 17: Heave motion amplitude spectra (normalised by H_s) for $\frac{1}{2}H_s k_p = 0.075$ and $k_p h =$ (a) 2.0, (b) 2.5 and (c) 3.0 showing — linear potential flow prediction, — ensemble average of experimental data and - - TD simulation.

the methodology established is more general. In day-to-day engineering practice, simple formulations must be accessible. Figure 18 provides an example of how a complex experimental data set of the form developed herein may be translated into a convenient empirical formulation.

The figure concerns the heave motion of the rectangular box, but any other quantity could have been selected. A Weibull distribution with probability density function

$$p(y) = \frac{m}{n} \left(\frac{y}{n}\right)^{m-1} e^{-(y/n)^m} \quad (3)$$

was used to obtain a fit to the data, where y is the variable under consideration (normalised heave motion ξ/d in this case), m is a shape parameter and n is a scale parameter. The solid black lines in Figure 18 show individual Weibull fits to the heave motion data for increasing sea state steepness. Adopting the average value of m between the three cases shown ($m = 2.175$), yields the dashed lines, which remain in close agreement with the experimental data (grey lines). The scale parameter can be approximated by a polynomial function of the form $n = 2.74 \left(\frac{1}{2}H_s k_p\right) - 5.18 \left(\frac{1}{2}H_s k_p\right)^2$. Adopting this polynomial expression for n and $m = 2.175$ predicts all experimental data in the range $10^{-3} \leq Q \leq 1$ within

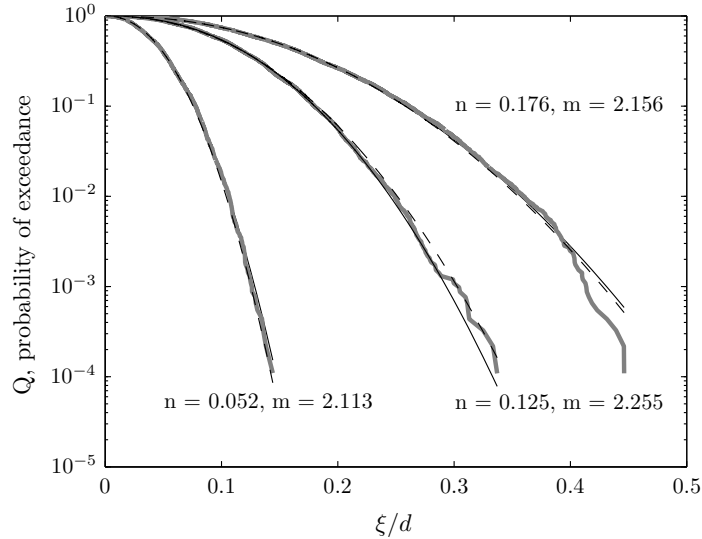


Figure 18: Weibull distributions of the heave motions due to irregular sea states with $k_p h = 2.0$ and $\frac{1}{2}H_s k_p = 0.02$ (left), 0.05 (centre) and 0.075 (right) showing — experimental data, - - - Weibull fit with n and m chosen independently for each sea state steepness and - . - Weibull fit with $m = 2.175$ independent of sea state steepness.

5%. From an engineering perspective, this type of function (two parameter fit) enables a sufficiently accurate and convenient motion prediction.

6. Concluding remarks

This paper presented an experimental investigation concerning both the excitation forcing and the heave motion of a rectangular box. In the context of regular waves, the existence of pronounced second harmonic forcing was demonstrated even for moderate wave steepnesses. This nonlinear content is particularly important in deeper water, where the second harmonic may account for up to 50% of the first harmonic force component. The presence of vortex shedding has a limited influence on the regular wave excitation forces, accounting for a forcing reduction of order 10%. However, considering the heaving motion in regular waves, the motion response was shown to be substantially lower than predicted using potential flow theory, particularly close to resonance. This effect is well studied and generally associated with the formation of vortex structures at sharp corners. In terms of nonlinear heave motion content, the findings established in a recent numerical investigation were largely reproduced. The presence of vortex-induced terms affected this nonlinear motion content in the long wave regime, but was shown to have little influence on the motion nonlinearities in the diffraction regime.

Advancing the work to steep irregular sea states, the excitation force time-histories were found to be strongly asymmetric as the local force minima were larger than the local maxima. For the steepest sea states, nonlinear amplifications in the measured force minima reached

up to 60%. This increase was attributed to considerable higher harmonic content, dominated by the second harmonic, and leading to rapidly evolving excitation forcing. Despite these force amplifications, which generally increase with the sea state steepness, the relative heave response in irregular waves generally decreases as the sea state steepness increases. The reasons for this are two-fold. First, the increase in the excitation forcing is primarily driven by high forcing frequencies, for which the large box inertia inhibits significant motions responses. Second, the presence of vortex-induced damping leads to substantial motion reductions, where the associated forcing terms broadly scale with the square of the heave velocity. On balance, the steepness-dependent damping outweighs the amplifications due to the excitation forcing nonlinearities, leading to smaller motion responses than predicted by (linear) potential flow. Incorporating a simple MOJS-type damping term within a time-domain simulation of the box captures the majority of this effect. However, the nature of this empirical damping term may also be a function of the sea state parameters, including the spectral peak period. Future work will hence focus on an improved physical understanding of vortex-induced damping, and how this can be incorporated reliably into day-to-day engineering models.

Acknowledgement

The first author would like to acknowledge the financial support provided through the BEIT Fellowship for Scientific Research, which has enabled this research. The work presented herein has also received financial support through UK EPSRC Grants EP/J010197/1 and EP/M019977/1. The authors would finally like to thank Mark Bruggemann and Mohamed Latheef for many fruitful discussions in the development of this research.

Alves, M., Sarmiento, A., Vicente, M. and Guérinel, M. (2011), Implementation and verification of a time domain model to simulate the dynamics of OWCs, *in* ‘Proceedings of the 9th European Wave and Tidal Energy Conference’, Southampton, UK.

Bai, W. and Eatock Taylor, R. (2009), ‘Fully nonlinear simulation of wave interaction with fixed and floating flared structures’, *Ocean Engineering* **36**(3–4), 223–236.

Baldock, T. E. and Swan, C. (1994), ‘Numerical calculations of large transient water waves.’, *Applied Ocean Research* **16**, 101–112.

Chen, L. F., Zang, J., Hillis, A. J., Morgan, G. C. J. and Plummer, A. R. (2014), ‘Numerical investigation of wave-structure interaction using openfoam’, *Ocean Engineering* (88), 91–109.

- Downie, M., Bearman, P. and Graham, J. (1988), ‘Effect of vortex shedding on the coupled roll response of bodies in waves’, *Journal of Fluid Mechanics* **189**, 243–264.
- Eatock Taylor, R. and Hung, S. (1987), ‘Second order diffraction forces on a vertical cylinder in regular waves’, *Applied Ocean Research* **9**(1), 19–30.
- Ferrant, P., Touzé, D. L. and Pelletier, K. (2003), ‘Non-linear time-domain models for irregular wave diffraction about offshore structures’, *International Journal for Numerical Methods in Fluids* **43**(10-11), 1257–1277.
- Guérinel, M., Zurkinden, A., Alves, M. and Sarmiento, A. (2013), Validation of a partially nonlinear time domain model using instantaneous Froude-Krylov and hydrostatic forces, *in* ‘Proceedings of the 10th European Wave and Tidal Energy Conference’, Aalborg Denmark.
- Hasselmann, K., Barnett, T., Bouws, E., Carlson, H., Cartwright, D., Enke, K., Ewing, J., Gienapp, H., Hasselmann, D., Kruseman, P. et al. (1973), Measurements of wind-wave growth and swell decay during the Joint North Sea Wave Project (JONSWAP), Technical report, Deutsches Hydrographisches Institut.
- Jefferys, E. (1984), ‘Simulation of wave power devices’, *Applied Ocean Research* **6**(1), 31–39.
- Johannessen, T. and Swan, C. (2001), ‘A laboratory study of the focusing of transient and directionally spread surface water waves’, *Proc. Roy. Soc. Lond. A* **457**, 971–1006.
- Johannessen, T. and Swan, C. (2003), ‘On the nonlinear dynamics of focused wave groups produced by the focusing of surface-water waves’, *Proc. Roy. Soc. Lond. A* **459**, 1021–1052.
- Kashiwagi, M. (2000), Non-linear simulations of wave-induced motions of a floating body by means of the mixed Eulerian-Lagrangian method, *in* ‘Proceedings of the Institution of Mechanical Engineers. Part C: Journal of Mechanical Engineering Science’, Vol. 214, pp. 841–855.
- Kim, M. and Yue, D. (1989), ‘The complete second-order diffraction solution for an axisymmetric body. Part 1: Monochromatic incident waves’, *Journal of Fluid Mechanics* **200**, 235–264.
- Kim, M. and Yue, D. (1990), ‘The complete second-order diffraction solution for an axisymmetric body: Part 2. Bichromatic incident waves and body motions’, *Journal of Fluid Mechanics* **211**, 557–593.

- Latheef, M. and Swan, C. (2013), ‘A laboratory study of wave crest statistics and the role of directional spreading’, *Proc. Roy. Soc. Lond. A* **469**.
- Lighthill, J. (1979), Waves and hydrodynamic loading, in ‘Proceedings of the Second International Conference on the Behaviour of Offshore Structures’, London, UK, pp. 1–40.
- Maiti, S. and Sen, D. (2001), ‘Nonlinear heave radiation forces on two-dimensional single and twin hulls’, *Ocean Engineering* **28**(8), 1031 – 1052.
- Molin, B. (1979), ‘Second-order diffraction loads upon three-dimensional bodies’, *Applied Ocean Research* **1**(4), 197–202.
- Morison, J., O’Brien, M., Johnson, J. and Schaaf, S. (1950), ‘The force exerted by surface waves on piles’, *Petroleum Transactions (AIME)* **189**, 149–154.
- Rodríguez, M., Spinneken, S. and Swan, C. (2016), ‘Nonlinear loading of a two-dimensional heaving box’, *Journal of Fluids and Structures* **60**, 80–96.
- Salvesen, N., Tuck, E. and Faltinsen, O. (1970), ‘Ship motions and sea loads’, *Transactions of the Society of Naval Architects and Marine Engineers* **78**, 421.
- Spinneken, J., Christou, M. and Swan, C. (2014), ‘Force-controlled absorption in a fully-nonlinear numerical wave tank’, *Journal of Computational Physics* **272**(0), 127–148.
- Stiassnie, M., Naheer, E. and Boguslavsky, I. (1984), ‘Energy losses due to vortex shedding from the lower edge of a vertical plate attacked by surface waves’, *Proc. Roy. Soc. Lond. A* **396**, 131–142.
- Sulisz, W. (1993), ‘Diffraction of second order surface waves by semisubmerged horizontal rectangular cylinder’, *Journal of Waterway, Port, Coastal, and Ocean Engineering* **119**(2), 160–171.
- Vire, A., Spinneken, J., Piggott, M., Pain, C. and Kramer, S. (2016), ‘Application of the immersed-body method to simulate wave-structure interactions’, *European Journal of Mechanics/B Fluids* **55**(2), 330–339.
- WAMIT (2013), *WAMIT User Manual: Version 7.0*, WAMIT Inc, www.wamit.com.
- Xue, M., Xü, H., Liu, Y. and Yue, D. K. P. (2001), ‘Computations of fully nonlinear three-dimensional wavebody interactions. part 1. dynamics of steep three-dimensional waves’, *Journal of Fluid Mechanics* **438**, 11–39.
- Yeung, R. W. and Ananthakrishan, P. (1992), ‘Oscillation of a floating body in a viscous fluid’, *Journal of Engineering Mathematics* **26**, 211–230.

Yeung, R. W. and Jiang, Y. (2014), ‘Shape effects on viscous damping and motion of heaving cylinders’, *Journal of Offshore Mechanics and Arctic Engineering* **136**(4).

Zhou, B., Ning, D., Teng, B. and Bai, W. (2013), ‘Numerical investigation of wave radiation by a vertical cylinder using a fully nonlinear HOBEM’, *Ocean Engineering* **70**, 1–13.

Appendix A. Experimental box setup

Figure A.1 shows a cross section of the rectangular box setup, where the arrow indicates the direction of wave propagation. The upstream face or left-hand side of the structure was made sufficiently large to prevent any ingress of water in the largest incident wave cases.

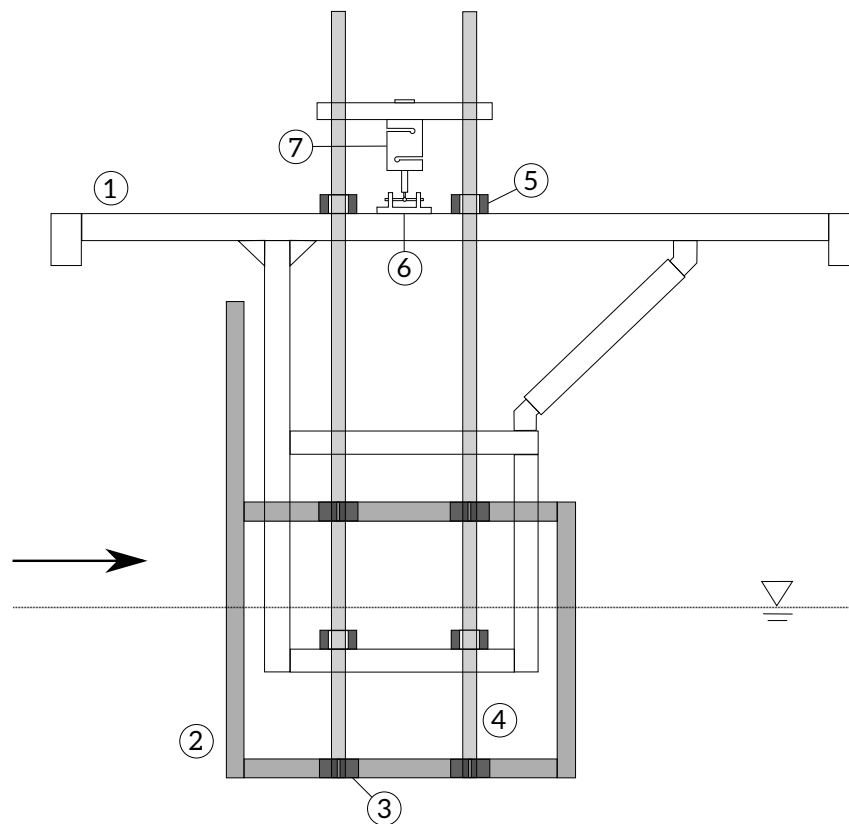


Figure A.1: Experimental setup for the fixed box problem, where the arrow indicates the direction of the incident waves. Key: (1) extruded aluminium superstructure, (2) rectangular box, (3) rigid clamp blocks, (4) 20 mm diameter stainless steel shafts, (5) low-friction linear ball bearings, (6) universal joint and (7) bidirectional load cell.

The experimental setup for the fixed-body excitation problem is as follows. The box is connected to an extruded aluminium superstructure fixed to the flume’s side wall. The connection between the rectangular box and the superstructure is made via a set of low friction linear ball bearings (part number 5 in Figure A.1). These bearings are arranged such that the total heave load is transferred to the load cell shown as part number 7. A universal

joint (part number 6) is used to ensure that all vertical loads are transferred through the load cell, while allowing for any small mis-alignments in the ball bearings. Two precision load cells were placed across the width of the box, with the total heave force resulting as the sum of the two measurements.

The second setup, appropriate to the heaving box problem, is very similar to that described above. For all test cases concerning the free-heave motion, the load cells (part number 7) were removed, and an additional set of ball bearings was introduced to ensure optimal alignment. The heave motion was then recorded using a high-accuracy laser displacement sensor of range 600 mm and resolution 80 μm .